

# Supplementary materials for Nontrivial temperature dependence of magnetic anisotropy in multiferroics $\text{Ba}_2\text{MnGe}_2\text{O}_7$

Shunsuke Hasegawa,<sup>1</sup> Shohei Hayashida,<sup>1</sup> Shinichiro Asai,<sup>1</sup>

Masato Matsuura<sup>2</sup>, Zaliznyak Igor<sup>3</sup> and Takatsugu Masuda<sup>1,4,5</sup>

<sup>1</sup> *Institute for Solid State Physics, The University of Tokyo, Chiba 277-8581, Japan*

<sup>2</sup> *Neutron Science and Technology Center,*

*Comprehensive Research Organization for Science and Society, Ibaraki 319-1106, Japan*

<sup>3</sup> *Condensed Matter Physics and Materials Science Department,*

*Brookhaven National Laboratory, Upton, NY 11973, USA*

<sup>4</sup> *Institute of Materials Structure Science,*

*High Energy Accelerator Research Organization, Ibaraki 305-0801, Japan*

<sup>5</sup> *Trans-scale Quantum Science Institute,*

*The University of Tokyo, Tokyo 113-0033, Japan*

(Dated: July 9, 2021)

# I. SPIN-WAVE CALCULATION FOR INELASTIC NEUTRON SCATTERING CROSS SECTION OF $\text{Ba}_2\text{MnGe}_2\text{O}_7$

The dynamical structure factor of  $\text{Ba}_2\text{MnGe}_2\text{O}_7$  is calculated by linear spin-wave theory using the recipe described in Ref. 2. We start from the following spin Hamiltonian:

$$\mathcal{H} = \mathcal{H}_1 + \mathcal{H}_2 + \mathcal{H}_3 + \mathcal{H}_4, \quad (1)$$

$$\mathcal{H}_1 = \sum_{i,j}^{ab} J_1 \mathbf{S}(\mathbf{R}_i^{(1)}) \cdot \mathbf{S}(\mathbf{R}_j^{(2)}) + \sum_{i,j}^c J_2 \mathbf{S}(\mathbf{R}_i^{(1)}) \cdot \mathbf{S}(\mathbf{R}_j^{(2)}), \quad (2)$$

$$\mathcal{H}_2 = D \sum_i (S^z(\mathbf{R}_i^{(r)}))^2, \quad (3)$$

$$\mathcal{H}_3 = J_N \sum_{i,j}^{ab} O_{XY}(\mathbf{R}_i^{(1)}) O_{XY}(\mathbf{R}_j^{(2)}) + J_{N2} \sum_{i,j}^c O_{XY}(\mathbf{R}_i^{(1)}) O_{XY}(\mathbf{R}_j^{(2)}), \quad (4)$$

$$O_{XY}(\mathbf{R}_i^{(r)}) = \cos(2\kappa_i^{(r)}) O_{xy}(\mathbf{R}_i^{(r)}) - \sin(2\kappa_i^{(r)}) O_2^2(\mathbf{R}_i^{(r)}),$$

$$O_{xy}(\mathbf{R}_i^{(r)}) = S^x(\mathbf{R}_i^{(r)}) S^y(\mathbf{R}_i^{(r)}) + S^y(\mathbf{R}_i^{(r)}) S^x(\mathbf{R}_i^{(r)}),$$

$$O_2^2(\mathbf{R}_i^{(r)}) = (S^x(\mathbf{R}_i^{(r)}))^2 - (S^y(\mathbf{R}_i^{(r)}))^2,$$

$$\mathcal{H}_4 = \sum_i a \left( (S^x(\mathbf{R}_i^{(r)}))^4 + (S^y(\mathbf{R}_i^{(r)}))^4 \right) + b (S^x(\mathbf{R}_i^{(r)}))^2 (S^y(\mathbf{R}_i^{(r)}))^2. \quad (5)$$

Here  $\mathbf{R}_i^{(r)}$  indicates a position vector of a spin with a site  $r$  in a unit cell  $i$ .  $\kappa_i^{(r)}$  is a tilt angle of  $\text{MnO}_4$  tetrahedron from the crystallographic  $[110]$  direction as shown in Fig. 1(a) in the main article. Exchange pathways in  $\mathcal{H}_1$  are shown in Fig. S1, and both of inplane interaction  $J_1$  and interplane interaction  $J_2$  are antiferromagnetic;  $J_1, J_2 > 0$ . The single-ion anisotropy

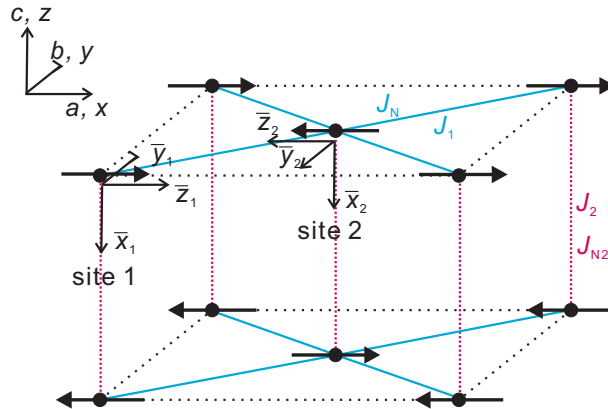


**Fig. S1** Magnetic structure of  $\text{Ba}_2\text{MnGe}_2\text{O}_7$  and relation between global coordinate  $x, y, z$  and local coordinate  $\bar{x}_i, \bar{y}_i, \bar{z}_i$  ( $i = 1, 2$ ).

of the 2nd order in  $\mathcal{H}_2$  is easy-plane type;  $D > 0$ . The inplane spin-nematic interaction  $J_N$  in  $\mathcal{H}_3$  is antiferromagnetic, and the interplane spin-nematic interaction  $J_{N2}$  is ferronematic;  $J_N > 0$  and  $J_{N2} < 0$ . The anisotropy of the 4th order in  $\mathcal{H}_4$  is biaxial anisotropy along  $x$  and  $y$  directions;  $a < 0$  and  $b > 0$ . The  $x$ ,  $y$ , and  $z$  axes in the global coordinate correspond to the crystallographic  $a$ -,  $b$ -, and  $c$ -axes. The relation between the local coordinate at each sublattice  $(\bar{x}, \bar{y}, \bar{z})$  and the global coordinate  $(x, y, z)$  is shown in Fig. S1. The spin operator in the global coordinate  $\mathbf{S}(\mathbf{R}_i^{(r)})$  and the one in the local coordinate  $\bar{\mathbf{S}}(\mathbf{R}_i^{(r)})$  is related by the unitary matrix  $U_r$  as follows:

$$\mathbf{S}(\mathbf{R}_i^{(r)}) = U_r^{-1} \bar{\mathbf{S}}(\mathbf{R}_i^{(r)}), \quad (6)$$

$$U_1^{-1} = \begin{pmatrix} 0 & 0 & 1 \\ 0 & 1 & 0 \\ -1 & 0 & 0 \end{pmatrix}, \quad (7)$$

$$U_2^{-1} = \begin{pmatrix} 0 & 0 & -1 \\ 0 & -1 & 0 \\ -1 & 0 & 0 \end{pmatrix}. \quad (8)$$

Holstein-Primakoff transformation yields the relation between local spin and boson operators:

$$\bar{S}^x(\mathbf{R}_i^{(r)}) = \sqrt{S/2}(a_i^{(r)} + a_i^{(r)\dagger}), \quad (9)$$

$$\bar{S}^y(\mathbf{R}_i^{(r)}) = -i\sqrt{S/2}(a_i^{(r)} - a_i^{(r)\dagger}), \quad (10)$$

$$\bar{S}^z(\mathbf{R}_i^{(r)}) = S - a_i^{(r)}a_i^{(r)\dagger}. \quad (11)$$

Fourier transformation of the boson operators are given by

$$a_{\mathbf{q}}^{(r)} = 1/\sqrt{N_u} \sum_i^{(r)} e^{-i\mathbf{q}\cdot\mathbf{R}_i^{(r)}} a_i^{(r)}, \quad (12)$$

$$a_{\mathbf{q}}^{(r)\dagger} = 1/\sqrt{N_u} \sum_i^{(r)} e^{i\mathbf{q}\cdot\mathbf{R}_i^{(r)}} a_i^{(r)\dagger}, \quad (13)$$

$$a_i^{(r)} = 1/\sqrt{N_u} \sum_{\mathbf{q}} e^{i\mathbf{q}\cdot\mathbf{R}_i^{(r)}} a_{\mathbf{q}}^{(r)}, \quad (14)$$

$$a_i^{(r)\dagger} = 1/\sqrt{N_u} \sum_{\mathbf{q}} e^{-i\mathbf{q}\cdot\mathbf{R}_i^{(r)}} a_{\mathbf{q}}^{(r)\dagger}. \quad (15)$$

The symbol ' in Eq. (14) and (15) means that the sums are taken over the 1st Brillouin zone. We transform the Hamiltonian in Eq. (1) into the boson representation, and the second-order terms are obtained straightforwardly:

$$\mathcal{H} = \sum_{\mathbf{q}}' \mathbf{v}_{\mathbf{q}}^{\dagger} L \mathbf{v}_{\mathbf{q}}, \quad (16)$$

$$\mathbf{v}_{\mathbf{q}} = (a_{\mathbf{q}}^{(1)}, a_{\mathbf{q}}^{(2)}, a_{-\mathbf{q}}^{(1)\dagger}, a_{-\mathbf{q}}^{(2)\dagger}), \quad (17)$$

$$L = \begin{pmatrix} A & Q_{\mathbf{q}} & P & B_{\mathbf{q}} \\ Q_{\mathbf{q}} & A & B_{\mathbf{q}} & P \\ P & B_{\mathbf{q}} & A & Q_{\mathbf{q}} \\ B_{\mathbf{q}} & P & Q_{\mathbf{q}} & A \end{pmatrix}, \quad (18)$$

$$A = 2(2J_1 + J_2)S + DS/2 - (-3K + 3a/2 + b/2)S^3, \quad (19)$$

$$B_{\mathbf{q}} = 2(2J_1\Gamma_{\mathbf{q}}^{ab} + J_2\Gamma_{\mathbf{q}}^c)S - Q_{\mathbf{q}}, \quad (20)$$

$$P = DS/2 + (-K - b/2)S^3, \quad (21)$$

$$K = 2(2J_N - J_{N2}) \sin^2(2\kappa), \quad (22)$$

$$Q_{\mathbf{q}} = 2 \cos^2(2\kappa)(4J_N\Gamma_{\mathbf{q}}^{ab} + 2J_{N2}\Gamma_{\mathbf{q}}^c)S^3, \quad (23)$$

$$\Gamma_{\mathbf{q}}^{ab} = 1/2 \left( \cos \frac{a}{2}(q_x + q_y) + \cos \frac{a}{2}(q_x - q_y) \right), \quad (24)$$

$$\Gamma_{\mathbf{q}}^c = \cos(cq_z). \quad (25)$$

From the commutation rule of boson operators  $a_{\mathbf{q}}^{(r)}$  and  $a_{\mathbf{q}'}^{(s)\dagger}$ , it is found that

$$[\mathbf{v}_{\mathbf{q}}, \mathbf{v}_{\mathbf{q}'}^{\dagger}] = \underline{N} \delta_{\mathbf{q}, \mathbf{q}'}, \quad (26)$$

$$\underline{N} = \begin{pmatrix} \underline{I} & 0 \\ 0 & -\underline{I} \end{pmatrix}. \quad (27)$$

Here  $\underline{I}$  is 2-dimensional unit matrix. A new matrix  $\mathcal{L}$  is defined

$$\mathcal{L} = L \cdot \underline{N}, \quad (28)$$

and the dispersion relations of the one-magnon is obtained by the characteristic equation,

$$\sum_j (\mathcal{L}_{n,j}(\mathbf{q}) - \delta_{n,j} \epsilon_n(\mathbf{q})) X_{n,j}(\mathbf{q})^* = 0, \quad (29)$$

where  $\hbar\omega_n^{\text{SWT}}(\mathbf{q}) = 2\epsilon_n(\mathbf{q})$ . The solutions are

$$\hbar\omega_{1,2}^{\text{SWT}}(\mathbf{q}) = 2\sqrt{(A \mp Q)^2 - (B \mp P)^2}, \quad (30)$$

$$\hbar\omega_{3,4}^{\text{SWT}}(\mathbf{q}) = -2\sqrt{(A \pm Q)^2 - (B \pm P)^2}. \quad (31)$$

Eqs. (30) and (31) correspond to creation and annihilation of magnons, respectively.  $\hbar\omega_1^{\text{SWT}}(\mathbf{q})$  is low energy mode, and  $\hbar\omega_2^{\text{SWT}}(\mathbf{q})$  is high energy mode. The eigenvectors give the matrix  $X$ , and its inversion is as follows

$$X^{-1} = \begin{pmatrix} \frac{B-P}{4c_1\epsilon_1}, & \frac{B+P}{4c_2\epsilon_2}, & \frac{-(B+P)}{4c_3\epsilon_2}, & \frac{-(B-P)}{4c_4\epsilon_1} \\ \frac{-(B-P)}{4c_1\epsilon_1}, & \frac{B+P}{4c_2\epsilon_2}, & \frac{-(B+P)}{4c_3\epsilon_2}, & \frac{B-P}{4c_4\epsilon_1} \\ \frac{A-Q-\epsilon_1}{4c_1\epsilon_1}, & \frac{-A-Q+\epsilon_2}{4c_2\epsilon_2}, & \frac{A+Q+\epsilon_2}{4c_3\epsilon_2}, & \frac{-A+Q-\epsilon_1}{4c_4\epsilon_1} \\ \frac{-A+Q+\epsilon_1}{4c_1\epsilon_1}, & \frac{-A-Q+\epsilon_2}{4c_2\epsilon_2}, & \frac{A+Q+\epsilon_2}{4c_3\epsilon_2}, & \frac{A-Q+\epsilon_1}{4c_4\epsilon_1} \end{pmatrix}. \quad (32)$$

Normalization condition required from the commutation rule of the boson is  $XNX^\dagger = \underline{N}$ , and it leads to

$$|c_1|^2 = \frac{1}{2 \left( \left( \frac{A-Q+\epsilon_1}{B-P} \right)^2 - 1 \right)}, \quad (33)$$

$$|c_2|^2 = \frac{1}{2 \left( \left( \frac{A+Q+\epsilon_2}{B+P} \right)^2 - 1 \right)}, \quad (34)$$

$$|c_3|^2 = \frac{1}{2 \left( \left( \frac{A+Q-\epsilon_2}{B+P} \right)^2 - 1 \right)}, \quad (35)$$

$$|c_4|^2 = \frac{1}{2 \left( \left( \frac{A-Q-\epsilon_1}{B-P} \right)^2 - 1 \right)}. \quad (36)$$

As is explained in the main article, in the case of a  $\text{Mn}^{2+}$  ion having a nuclear spin  $I = 5/2$ , hyperfine coupling between the nuclear and electron spins induces a low energy gap in addition to the magnetic anisotropy gap. The excitation energy modified by the hyperfine coupling is:

$$\hbar\omega_n(\mathbf{q})^2 = (\hbar\omega_n^{\text{SWT}}(\mathbf{q}))^2 + (\Delta^{\text{HF}})^2, \quad (37)$$

where  $\hbar\omega_n(\mathbf{q})$  is the magnon dispersion of  $\text{Ba}_2\text{MnGe}_2\text{O}_7$  and  $\Delta^{\text{HF}}$  is the hyperfine gap [3, 4].  $\epsilon_n$  in Eqs. (32)-(36) is replaced by  $\epsilon'_n$ , where

$$\epsilon'_n = 1/2\hbar\omega_n(\mathbf{q}). \quad (38)$$

Then the matrix  $X$  becomes

$$X'^{-1} = \begin{pmatrix} \frac{B-P}{4c'_1\epsilon'_1}, & \frac{B+P}{4c'_2\epsilon'_2}, & \frac{-(B+P)}{4c'_3\epsilon'_2}, & \frac{-(B-P)}{4c'_4\epsilon'_1} \\ \frac{-(B-P)}{4c'_1\epsilon'_1}, & \frac{B+P}{4c'_2\epsilon'_2}, & \frac{-(B+P)}{4c'_3\epsilon'_2}, & \frac{B-P}{4c'_4\epsilon'_1} \\ \frac{A-Q-\epsilon'_1}{4c'_1\epsilon'_1}, & \frac{-A-Q+\epsilon'_2}{4c'_2\epsilon'_2}, & \frac{A+Q+\epsilon'_2}{4c'_3\epsilon'_2}, & \frac{-A+Q-\epsilon'_1}{4c'_4\epsilon'_1} \\ \frac{-A+Q+\epsilon'_1}{4c'_1\epsilon'_1}, & \frac{-A-Q+\epsilon'_2}{4c'_2\epsilon'_2}, & \frac{A+Q+\epsilon'_2}{4c'_3\epsilon'_2}, & \frac{A-Q+\epsilon'_1}{4c'_4\epsilon'_1} \end{pmatrix}, \quad (39)$$

where

$$|c'_1|^2 = \frac{1}{2 \left( \left( \frac{A-Q+\epsilon'_1}{B-P} \right)^2 - 1 \right)}, \quad (40)$$

$$|c'_2|^2 = \frac{1}{2 \left( \left( \frac{A+Q+\epsilon'_2}{B+P} \right)^2 - 1 \right)}, \quad (41)$$

$$|c'_3|^2 = \frac{1}{2 \left( \left( \frac{A+Q-\epsilon'_2}{B+P} \right)^2 - 1 \right)}, \quad (42)$$

$$|c'_4|^2 = \frac{1}{2 \left( \left( \frac{A-Q-\epsilon'_1}{B-P} \right)^2 - 1 \right)}. \quad (43)$$

Then the dynamical structure factor is represented by

$$S^{\alpha\beta}(\mathbf{q}, \omega) = \sum_n S^{(n),\alpha\beta}(\mathbf{q}) \delta(\hbar\omega - \hbar\omega_n(\mathbf{q})), \quad (44)$$

$$S^{(n),\alpha\beta}(\mathbf{q}) = S/4 \sum_{r,s=1}^2 W'_{r,\alpha}{}^{(n)}(\mathbf{q}) W'_{s,\beta}{}^{(n)}(\mathbf{q})^*, \quad (45)$$

$$W'_{r,\alpha}{}^{(n)}(\mathbf{q}) = V_{r,\alpha}^- X_{r,n}'^{-1} + V_{r,\alpha}^+ X_{r+2,n}'^{-1}(\mathbf{q}), \quad (46)$$

$$V_{r,\alpha}^\pm = (U_r^{-1})_{\alpha,x} \pm i(U_r^{-1})_{\alpha,y}. \quad (47)$$

The inelastic neutron scattering cross section is expressed as follows:

$$\frac{d^2\sigma}{d\Omega dE'} = \frac{(g_n r_0/2)^2 k'}{2\pi\hbar} \frac{1}{k} |gF(\mathbf{q})|^2 \langle n_{\mathbf{q}} + 1 \rangle \sum_{\alpha,\beta=x,y,z} (\delta_{\alpha\beta} - \hat{\kappa}_\alpha \hat{\kappa}_\beta) S^{\alpha\beta}(\mathbf{q}, \omega), \quad (48)$$

$$\langle n_{\mathbf{q}} + 1 \rangle = \frac{\exp(\hbar\omega_n(\mathbf{q})/k_B T)}{\exp(\hbar\omega_n(\mathbf{q})/k_B T) + 1}. \quad (49)$$

Here,  $g_n$  is  $g$ -factor of neutron,  $r_0$  is the classical radius of electron,  $k$  is the wave number of the incident neutron,  $k'$  is the wave number of the scattered neutron,  $g$  is Landé's  $g$ -factor,  $F(\mathbf{q})$  is the magnetic form factor of the  $\text{Mn}^{2+}$  ion [5], and  $\hat{\kappa}_\alpha$  is the  $\alpha$  component of the unit scattering vector.  $\langle n_{\mathbf{q}} \rangle$  is the temperature factor of the boson.

The anisotropy energies at the magnetic  $\Gamma$  point,  $\mathbf{q}_\Gamma = (1, 0, 1/2)$ , for the  $T_1$  and  $T_2$  modes are

$$\Delta_1^{\text{SWT}} = \hbar\omega_1(\mathbf{q}_\Gamma) = 4S^2 \sqrt{2(2J_1 + J_2 + D/2)(8J_N + 4J_{N2} \cos(4\kappa) - 3a/2)}, \quad (50)$$

$$\Delta_2^{\text{SWT}} = \hbar\omega_2(\mathbf{q}_\Gamma) = 4S \sqrt{(2J_1 + J_2)D} \quad (51)$$

in the lowest order of  $S$ . In Eq. (50)  $4\kappa = 90.4^\circ$ , and  $4J_{N2} \cos(4\kappa)$  is negligible. As shown in Fig. 4(a) in the main article,  $\Delta_2^{\text{SWT}}$  is scaled by the sublattice moment, meaning that the single-ion anisotropy  $D$  is temperature independent. This indicates that the coefficient  $a$  and  $b$  in the single-ion anisotropy with the 4th order term are also temperature independent, since the origins of the coefficients are commonly the products of matrix elements of the orbital angular momentum.  $\Delta_1^{\text{SWT}}$  in Fig. 4(b) in the main article is strongly dependent on the temperature. This suggests that the temperature independent component in  $\Delta_1^{\text{SWT}}$  is small, and  $a$  is negligible. Then,  $\Delta_1^{\text{SWT}}$  is approximated as

$$\Delta_1^{\text{SWT}} \sim 16S^2 \sqrt{J_N(2J_1 + J_2 + D/2)}. \quad (52)$$

The coefficient  $b$  does not appear in the leading term of the anisotropy energy of axial type  $\Delta_1^{\text{SWT}}$  in Eq. (50). Thus, the single-ion anisotropy of the 4th order in Eq. (5) can be neglected for the discussion of the magnetic anisotropy of axial type such as spin-flop field and the anisotropy gap in the INS spectrum.

## II. FIELD DERIVATIVE OF MAGNETIZATION

In this section we estimate the spin-nematic interaction from the spin-flop field  $H_{\text{SF}}$ . The field derivatives of magnetization  $dM/dH$ s in the field applied along the easy axis, [110], at 0.5 K, 1.8 K, and 2.5 K are shown in Figs. S2(a), S2(c) and S2(e), respectively. We defined the peak of the  $dM/dH$  as  $H_{\text{SF}}$ , and they are shown in Fig. 2(c) in the main article. As for  $T = 0.05$  and 0.9 K, we estimated  $H_{\text{SF}}$  from the extrapolation and interpolation as shown in Fig. S3. They are used for the estimate of  $\Delta_1^{\text{SWT}}$  at the temperatures.

In order to calculate  $dM/dH$ , we numerically calculate the mean-field energy of the system,  $E^{\text{MF}}$ , under the assumption that the spins are restricted in the crystallographic  $ab$  plane as shown in Fig. S4. The spin structure is characterized by the angle between the  $a$  axis and the spin direction,  $\phi_r$ . We consider the isotropic Heisenberg and spin-nematic

terms as follows:

$$E^{\text{MF}} = E_1^{\text{MF}} + E_2^{\text{MF}} + E_3^{\text{MF}}, \quad (53)$$

$$E_1^{\text{MF}} = \sum_{i,j}^{ab} J_1 \mathbf{S}(\mathbf{R}_i^{(1)}) \cdot \mathbf{S}(\mathbf{R}_j^{(2)}) + \sum_{i,j}^c J_2 \mathbf{S}(\mathbf{R}_i^{(1)}) \cdot \mathbf{S}(\mathbf{R}_j^{(2)}) \quad (54)$$

$$E_2^{\text{MF}} = J_N \sum_{i,j}^{ab} O_{XY}(\mathbf{R}_i^{(1)}) O_{XY}(\mathbf{R}_j^{(2)}) \quad (55)$$

$$O_{XY}(\mathbf{R}_i^{(r)}) = \cos(2\kappa_i^{(r)}) O_{xy}(\mathbf{R}_i^{(r)}) - \sin(2\kappa_i^{(r)}) O_2^2(\mathbf{R}_i^{(r)})$$

$$O_{xy}(\mathbf{R}_i^{(r)}) = S^x(\mathbf{R}_i^{(r)}) S^y(\mathbf{R}_i^{(r)}) + S^y(\mathbf{R}_i^{(r)}) S^x(\mathbf{R}_i^{(r)})$$

$$O_2^2(\mathbf{R}_i^{(r)}) = (S^x(\mathbf{R}_i^{(r)}))^2 - (S^y(\mathbf{R}_i^{(r)}))^2$$

$$E_3^{\text{MF}} = -g\mu_B \sum_{i,k} \mathbf{S}(\mathbf{R}_i^{(r)}) \cdot \mathbf{H} \quad (56)$$

$$\mathbf{S}(\mathbf{R}_i^{(r)}) = S(\cos \phi_r, \sin \phi_r, 0). \quad (57)$$

From the discussion in the Section I, we neglect  $J_{N2}$ ,  $a$  and  $b$  in the original Hamiltonian in

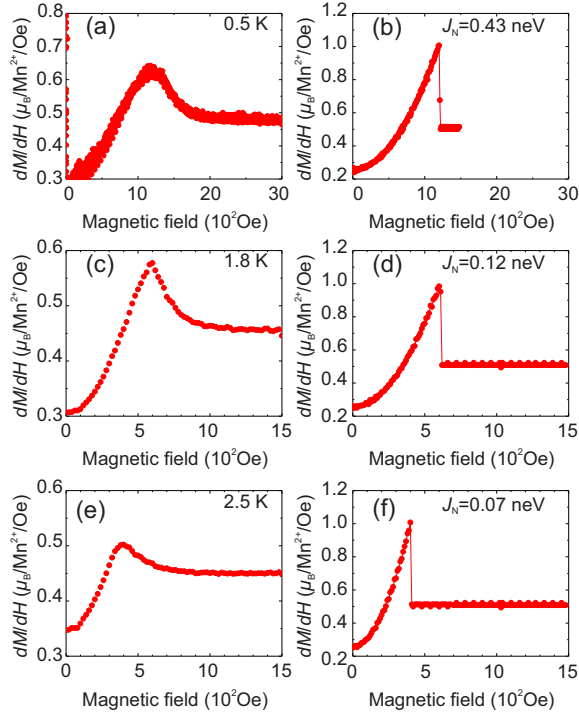


**Fig. S2** Field derivatives of magnetization ( $dM/dH$ ) in the field applied along the [110] direction. (a) Measured  $dM/dH$  at 0.5 K [6]. (b) Calculated  $dM/dH$  with  $J_N = 0.43$  neV. (c) Measured  $dM/dH$  at 1.8 K. (d) Calculated  $dM/dH$  with  $J_N = 0.12$  neV. (e) Measured  $dM/dH$  at 2.5 K. (f) Calculated  $dM/dH$  with  $J_N = 0.07$  neV.

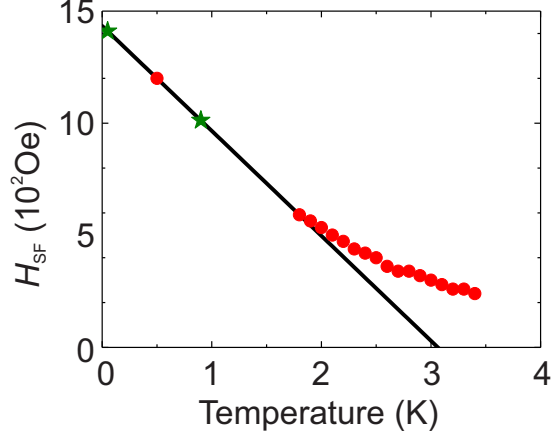


**Fig. S3** Estimate of the spin-flop field at 0.05 and 0.9 K.

Eq. (1). We use the magnitudes of the spin moments at 0.5, 1.8 and 2.5 K which are obtained from the present experiment. We use  $J_1 = 27.8 \mu\text{eV}$ ,  $J_2 = 1 \mu\text{eV}$  and  $g = 2$ .  $J_N$  is a free parameter. We numerically calculate  $E^{\text{MF}}$  of the spin configuration with a  $J_N$  for a set of random parameters  $\phi_r$ , and we find the spin structure having the minimum energy.  $dM/dH$ s are calculated for the spin structures with sequential  $J_N$ s with a step of 0.001 neV. The best  $dM/dH$ s that reproduce the spin-flop fields at  $J_N$ s are obtained at the temperatures, and they are shown in Figs. S2(b), S2(d), and S2(f).  $J_N$  is strongly dependent on temperature as shown in Fig. S5. The relation between  $H_{\text{SF}}$  and  $J_N$  is shown in Fig. S6. The positive correlation is found, and  $H_{\text{SF}}$  is a good index for the energy of the axial magnetic anisotropy.

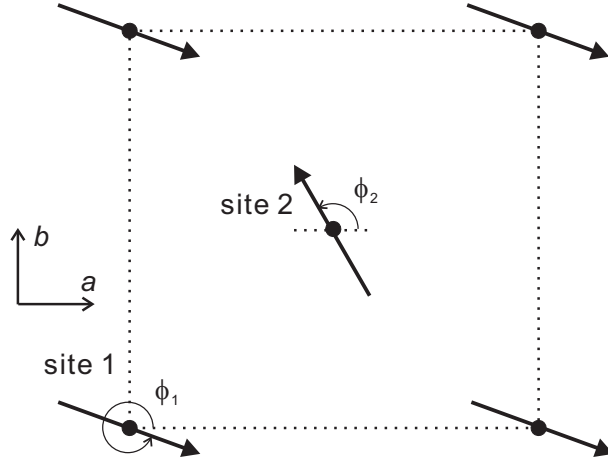


**Fig. S4** Spin configuration for the calculation of the energy.

**Table SI**  $D$  and  $\Gamma$  estimated from INS spectra.

$T$ (K)	0.05	0.9	1.8	2.5
$D$ ( $\mu\text{eV}$ )	2.4	2.4	2.2	2.1
$\Gamma$ ( $\mu\text{eV}$ )	6.7	10	16	19

### III. ANALYSIS OF INELASTIC NEUTRON SCATTERING SPECTRA

Inelastic neutron scattering spectra in Fig. 3(f) in the main article is analyzed by Eqs. (44) and (48). The broadening of the peak is due to both instrumental resolution and finite lifetime of magnon. Here we do not distinguish them, and we introduce Gaussian function. The  $\delta$  function in Eq. (44) is, then, replaced by

$$\delta(\hbar\omega - \hbar\omega_n(\mathbf{q})) \rightarrow \frac{1}{\sqrt{\pi}\Gamma} \exp\left(-\left(\frac{\hbar\omega - \hbar\omega_n(\mathbf{q})}{\Gamma}\right)^2\right), \quad (58)$$

where  $\Gamma$  is the broadening factor. As derived in Eqs. (37) and (52),  $J_N$ ,  $J_1$ ,  $J_2$ ,  $D$  and  $\Delta^{\text{HF}}$  contribute to the energy gap.  $N_2^{\text{eff}}$ ,  $a$ , and  $b$  are irrelevant, and we fix  $N_2^{\text{eff}} = a = b = 0$ . We use  $J_1 = 27.8 \mu\text{eV}$  and  $J_2 = 1 \mu\text{eV}$  from previous study [6]. As for  $J_N$  in Eq. (5) we use the values estimated from the spin-flop field. The free parameters are  $D$  in Eq. (3),  $\Delta^{\text{HF}}$  in Eq. (37), and  $\Gamma$  in Eq. (58). Fits to the data are shown in Figs. 3(f) in the main article, and the obtained parameters are summarized in Table SI.

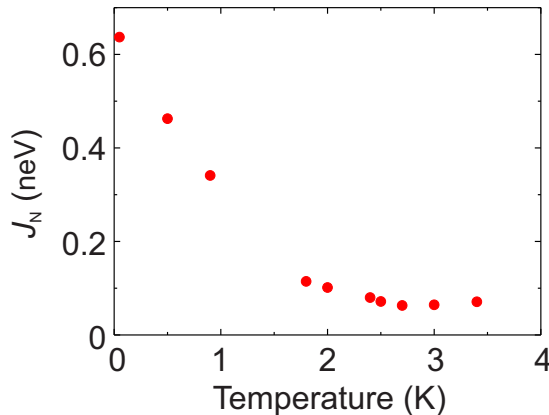


**Fig. S5** Temperature variation of evaluated spin-nematic interaction  $J_N$  from the analysis of  $dM/dH$ .

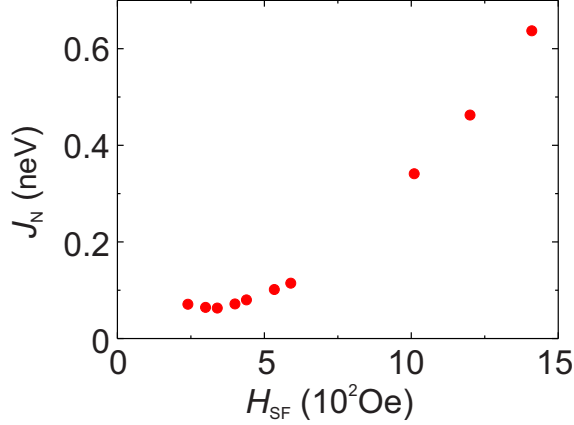


**Fig. S6** Relation between spin-flop field  $H_{\text{SF}}$  and spin-nematic interaction  $J_N$ .

#### IV. TEMPERATURE DEPENDENCE OF $\Delta^{\text{HF}}$

The energy gap induced by hyperfine coupling between nuclear spin and electron spin is expressed as follows:

$$\Delta^{\text{HF}} = \sqrt{(\chi_n(T)/\chi_c(T))} Ag\mu_B \langle S(T) \rangle. \quad (59)$$

Here  $\chi_c(T)$  is the susceptibility of electron spin in the field applied along the  $c$  axis, and  $A$  is the hyperfine coupling constant. The  $c$  axis is perpendicular to the magnetic easy axis, and  $\chi_c(T)$  is almost independent on the temperature. Then  $\chi_c = 0.25$  emu/mole [6] is used.  $\chi_n(T)$  is the susceptibility of nuclear spin, yielding to Curie law

$$\chi_n(T) = \frac{C}{T} \quad (60)$$

$$C = \frac{Ng_N^2\mu_N^2 I(I+1)}{3k_B}. \quad (61)$$

$(\Delta^{\text{HF}}/\langle S(T) \rangle)^2$  is proportional to  $\chi_n(T)$ , and it is shown in Fig. S7. It is estimated that  $A = 240$  kOe. In Mn materials,  $A$  is reported to be 259 kOe [3, 7], and our value is close to it.

---

[1] A. Sazonov *et al.*, Inorg. Chem. **57**, 5089 (2018).

[2] R.S. Fishman, J. A. Fernandez-Baca, and T. Rõõm, *Spin-Wave Theory and its Applications to Neutron Scattering and THz Spectroscopy* (IOP Concise Physics, A Morgan and Claypool Publication).

- [3] I. A. Zaliznyak, N. N. Zolin, and S. V. Petrov, JETP Lett. **64**, 473 (1996).
- [4] L. A. Prozorova *et al.*, JETP **85**, 1035 (1997).
- [5] A. J. C. Wilson and E. Prince, *International Tables for Crystallography*, (Kluwer Academic Publishers, Dordrecht/Boston/London, 2004) Vol. C, 3rd ed.
- [6] T. Masuda *et al.*, Phys. Rev. B **81**, 100402 (2010).
- [7] A. M. Clogston *et al.*, Phys. Rev. **117**, 1222 (1960).

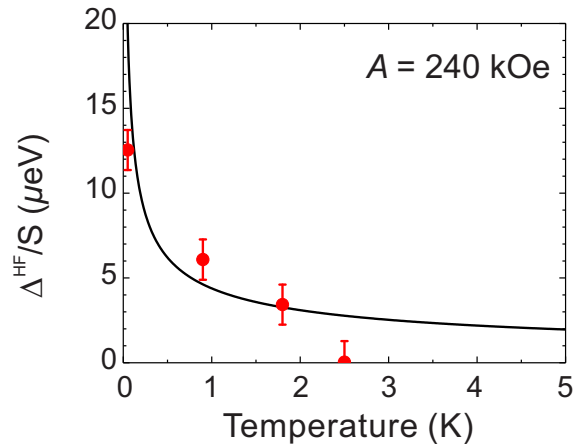


**Fig. S7** Temperature dependence of  $\Delta^{\text{HF}}/\langle S(T) \rangle$  estimated from INS spectra.

# Nontrivial temperature dependence of magnetic anisotropy in multiferroics $\text{Ba}_2\text{MnGe}_2\text{O}_7$

Shunsuke Hasegawa,<sup>1</sup> Shohei Hayashida,<sup>1</sup> Shinichiro Asai,<sup>1</sup>

Masato Matsuura<sup>2</sup>, Zaliznyak Igor<sup>3</sup> and Takatsugu Masuda<sup>1,4,5</sup>

<sup>1</sup> *Institute for Solid State Physics, The University of Tokyo, Chiba 277-8581, Japan*

<sup>2</sup> *Neutron Science and Technology Center,*

*Comprehensive Research Organization for Science and Society, Ibaraki 319-1106, Japan*

<sup>3</sup> *Condensed Matter Physics and Materials Science Department,*

*Brookhaven National Laboratory, Upton, NY 11973, USA*

<sup>4</sup> *Institute of Materials Structure Science,*

*High Energy Accelerator Research Organization, Ibaraki 305-0801, Japan*

<sup>5</sup> *Trans-scale Quantum Science Institute,*

*The University of Tokyo, Tokyo 113-0033, Japan*

(Dated: July 9, 2021)

## Abstract

We measured the temperature dependences of the static magnetization and the spin excitation in a square-lattice multiferroics  $\text{Ba}_2\text{MnGe}_2\text{O}_7$ . An anisotropy gap of the observed low energy mode is scaled by electric polarization rather than a power of sublattice moment. Spin nematic interaction in effective spin Hamiltonian, which is equivalent to interaction of electric polarization, is responsible for the easy-axis anisotropy. The nontrivial behavior of the anisotropy gap can be rationalized as change of the hybridized  $d$ - $p$  orbital with temperature, leading to the temperature dependence of the spin nematic interaction.

Spin-driven multiferroics [1–3] have been extensively studied since the discovery of an enhanced magnetoelectric (ME) effect in  $\text{TbMnO}_3$  [4]. Through spin-orbit coupling (SOC), a spin order induces a change of charge distribution, leading to emergence of electric polarization. The microscopic mechanisms of the multiferroics are categorized into three types [1]: the spin current [5], the exchange striction [6] and the spin dependent  $d$ - $p$  hybridization [7, 8]. A notable feature of the latter is that hybridized  $d$  and  $p$  orbitals of magnetic ion and ligand are modulated by spin states via SOC, and this induces an electric polarization. The relation between the electric polarization  $\mathbf{P}$  and the spin moment  $\mathbf{S}$  is locally described as  $\mathbf{P} = \Lambda \sum_i (\mathbf{S} \cdot \mathbf{e}_i)^2 \mathbf{e}_i$ , where  $\mathbf{e}_i$  is the bonding vector between the magnetic ion and the  $i$ -th ligand. Coefficient  $\Lambda$  is determined by SOC and transfer integrals between the magnetic ion and ligands. The mechanism has been identified in  $\text{CuFeO}_2$  [7], åkermanite compounds [9–11],  $\text{Cu}_2\text{OSeO}_3$  [12, 13] and rare-earth ferrobates [14, 15]. Since the direction of the local spin moment determines the direction of the electric polarization, magnetic anisotropy plays a key role in forming multiferroic structure, *i.e.*, the simultaneous structures of the spin and polarization [10, 11, 16]. The magnitude of the anisotropy gives the energy scale for the control of the magnetism by the electric field as well as magnetic field, which was tested in  $\text{Cu}_2\text{OSeO}_3$  [13] and an åkermanite  $\text{Ba}_2\text{CoGe}_2\text{O}_7$  [17]. Although the temperature ( $T$ ) dependences of the anisotropy gap in magnon spectrum in a conventional magnet scales as a power of the sublattice magnetic moment [18, 19], it may not be the case for the multiferroics. The change of the polarization with  $T$  affects the spin-interaction parameters through the  $d$ - $p$  hybridization, which might lead to a nontrivial behavior in  $T$  dependence of the anisotropy and a low-energy spin dynamics near the magnetic  $\Gamma$  point.

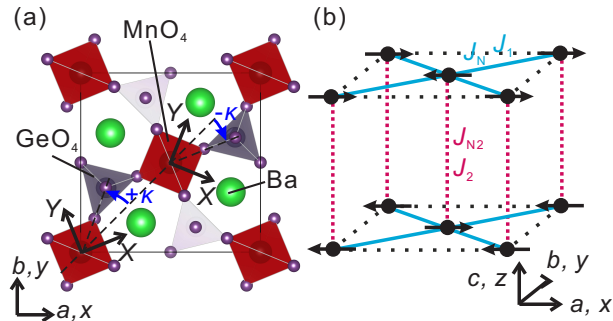


FIG. 1: (a) Crystal structure of  $\text{Ba}_2\text{MnGe}_2\text{O}_7$ .  $\text{MnO}_4$  tetrahedra are alternatively tilted by the characteristic angle of  $\kappa$ . (b) Magnetic structure of  $\text{Ba}_2\text{MnGe}_2\text{O}_7$  and the exchange pathways.

We focus on a multiferroic  $\text{Ba}_2\text{MnGe}_2\text{O}_7$  [20] which is isostructural to  $\text{Ba}_2\text{CoGe}_2\text{O}_7$  but is distinct in that the effect of the crystal electric field on the isotropic charge distribution of the half-filled shell of  $\text{Mn}^{2+}$  ion is small. Hence, weak spin-nematic interaction originating from the  $d$ - $p$  hybridization with the ligand, which can be sensitive to small change of the orbitals with the temperature, is the main source of magnetic anisotropy. The crystal structure is tetragonal and the space group is  $P\bar{4}2_1m$  [21], as shown in Fig. 1(a).  $\text{Mn}^{2+}$  ions carrying spin  $S = 5/2$  form a square lattice in the  $ab$  plane. The magnetic susceptibility exhibits a typical behavior of a classical square-lattice Heisenberg antiferromagnet with the interaction of  $26 \mu\text{eV}$ . At the Néel temperature ( $T_N$ ) of 4 K, a magnetic long-range order with the propagation vector of  $(1, 0, 1/2)$  sets in, and a collinear spin structure in which the spins lie in the  $ab$  plane is realized as shown in Fig. 1(b). The magnitude of the magnetic moment at 1.7 K is  $4.66 \mu_B$  and is close to the saturation moment. The electric polarization appears below  $T_N$  when the magnetic field is applied along the crystallographic  $[110]$  direction [9] and the origin of the multiferroicity is explained by the spin dependent  $d$ - $p$  hybridization mechanism, which is also the main source of  $\text{Mn}^{2+}$  spin anisotropy. Inelastic neutron scattering (INS) experiment at 1.7 K using conventional triple-axis spectrometer with the energy resolution of 0.1 meV determined the main parameters in the presumed isotropic spin Hamiltonian; the nearest-neighbor interaction in the  $ab$  plane  $J_1$  is  $27.8 \mu\text{eV}$ , and the interplane interaction  $J_2$  is  $1.0 \mu\text{eV}$ . To reveal the magnetic anisotropy in the low-energy dynamics and its possible nontrivial behavior in  $T$  dependence, we study the detailed field - temperature ( $H - T$ ) phase diagram and inelastic neutron scattering spectra using a state-of-art spectrometer with ultra-high resolution.

Single crystals were grown in  $\text{O}_2$  atmosphere by the floating zone method. The magnetization was measured by a commercial SQUID magnetometer. The INS experiment was carried out using the near backscattering spectrometer DNA in J-PARC MLF [22]. The horizontal scattering plane was the  $ac$  plane, and the final energy of neutrons  $E_f$  was set to 2.084 meV by using Si (111) analyzer. The energy resolution was estimated to be  $5.5 \mu\text{eV}$  in FWHM at an elastic condition of incoherent scattering near  $\mathbf{Q} = (1, 0, 1/2)$ . A dilution refrigerator was used to cool the sample to 0.05 K.

In the field derivative of the magnetization  $dM/dH$ , the fourfold rotational symmetry in the  $ab$  plane which is a characteristic feature of the spin-nematic interaction as demonstrated in  $\text{Ba}_2\text{CoGe}_2\text{O}_7$  [11] is observed [Fig. 2(a)]. Enhancements of  $dM/dH$  at  $H = 600$  Oe for

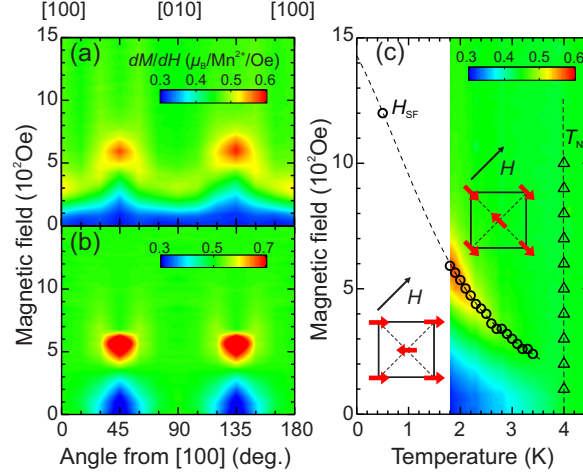


FIG. 2: Field derivative of magnetization ( $dM/dH$ ). (a) False color plot of  $dM/dH$  measured in the field applied in the  $ab$  plane at 1.8 K. The horizontal axis is the angle between  $[100]$  and the field directions. (b) False color plot of calculated  $dM/dH$  in the  $ab$  plane. (c) Measured  $H - T$  map of  $dM/dH$  for  $H \parallel [110]$ .  $dM/dH$  curves measured at typical temperatures are shown in Supplementary Fig. S3. Black circles indicate  $H_{\text{SF}}$  determined by the peak tops of  $dM/dH$ . A circle at 0.5 K indicates  $H_{\text{SF}}$  reported in previous study [20]. Triangles indicate Néel temperatures evaluated from the  $T$  dependence of the magnetization. The representative descriptions of the magnetic structures below and above  $H_{\text{SF}}$  are inserted.

$H \parallel [110]$  and  $[\bar{1}10]$  are due to a spin-flop (SF) transition. The existence of the biaxial SF transitions suggests that the easy axes are  $[100]$  and  $[010]$ . The corresponding electric polarization structure is antiferroelectric where  $\mathbf{P}$  is along the  $c$  axis [9]. The SF field drastically decreases with the increasing  $T$  as shown in  $H - T$  phase diagram in Fig. 2(c), which contrasts with conventional antiferromagnets exhibiting approximately  $T$  independent behavior at  $T < T_{\text{N}}$ .

Figure 3(a) shows the INS spectrum measured at 0.05 K. Two dispersive modes with the boundary energy of 0.55 meV and with gaps  $\sim 0.04$  meV and  $\sim 0.1$  meV are clearly observed. The overall energy scale is consistent with the previous study [20]. It is remarkable that the two dispersive modes with finite gaps are clearly resolved, which was not the case in previous study because of the relaxed energy resolution. Anisotropy gaps ( $E_g$ ) of the low- and high-energy modes, T1 and T2, respectively, at the magnetic  $\Gamma$  point,  $\mathbf{Q} = (1, 0, 1/2)$ ,

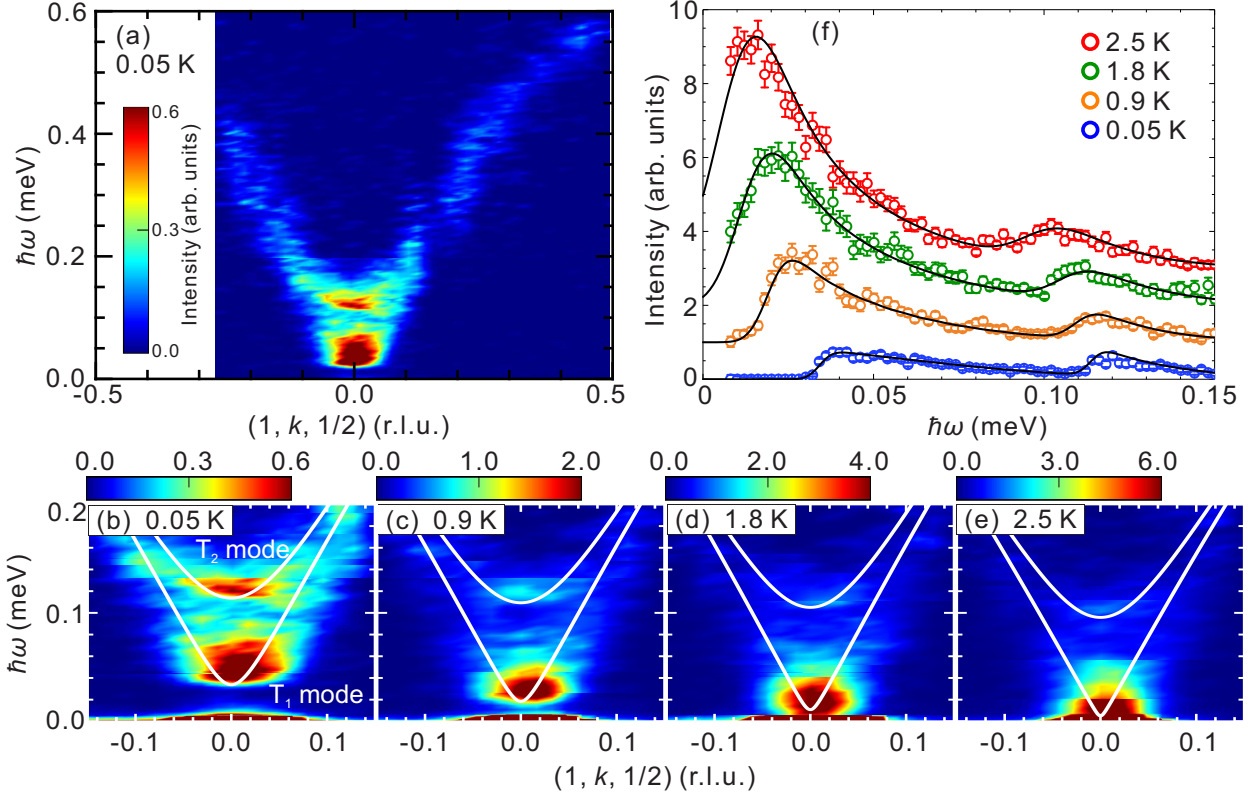


FIG. 3: Inelastic neutron scattering (INS) spectra. (a) False color plot of the INS spectrum measured at 0.05 K projected onto the  $\hbar\omega$ - $(1, k, 1/2)$  plane. The spectrum is integrated in the range of  $0.9 \leq h \leq 1.1$  and  $0.45 \leq l \leq 0.55$ . White solid curves are calculated magnon-dispersions. (b)-(e) The INS spectra focused on the low-energy range measured at (b) 0.05 K, (c) 0.9 K, (d) 1.8 K and (e) 2.5 K. White solid curves are calculated dispersions. (f) Temperature evolution of constant- $\mathbf{q}$  cuts at  $\mathbf{Q} = (1, 0, 1/2)$ ; data at different temperature are vertically offset. Coherent elastic scattering is subtracted for each temperature. The spectra are integrated in the range of  $-0.035 \leq k \leq 0.035$ . The asymmetric peak shape results from the wave vector resolution. Black solid curves are the calculated magnon cross section.

are identified at  $36 \mu\text{eV}$  and  $113 \mu\text{eV}$ . The latter is consistent with the value reported in previous ESR study [23].  $E_g$  of the  $T_1$  mode ( $E_{g1}$ ) is drastically suppressed with the increase of  $T$  as shown in Figs. 3(b)-3(e), while  $E_g$  of the  $T_2$  mode ( $E_{g2}$ ) is moderately suppressed. The intensities of the modes at the  $\Gamma$  point increases with the increasing  $T$  according to the thermal balance factor, as shown in Fig. 3(f).

The  $T$  dependences of  $E_{g2}$  and the sublattice moment  $g\mu_B\langle S \rangle$  are shown in Fig. 4(a). The

change of  $E_{g_2}$  in the measurement range is small, and it scales as  $g\mu_B\langle S \rangle$ . The behavior is consistent with conventional antiferromagnets where single-ion anisotropy is dominated by quadratic forms of spin operators [18, 19]. In contrast,  $E_{g_1}$  in Fig. 4(b) increases continuously with the decrease of  $T$ , and it cannot be scaled either by the sublattice moment or any power of it. This indicates that the  $T_1$  mode is not purely magnetic dynamics of electronic spin, but is hybridized with some other degrees of freedom.

We calculate the  $dM/dH$  curves and the dynamical structure factor of neutron scattering using the leading-order  $1/S$  expansion of the following Hamiltonian:

$$\mathcal{H} = \sum_{i,j} J_1 \mathbf{S}_i \cdot \mathbf{S}_j + \sum_{k,l} J_2 \mathbf{S}_k \cdot \mathbf{S}_l + \sum_i \{D(S_i^z)^2 + g\mu_B \mathbf{S}_i \cdot \mathbf{H}\} + \mathcal{H}_N, \quad (1)$$

$$\mathcal{H}_N = \sum_{i,j} J_N O_i^{XY} O_j^{XY}, \quad (2)$$

where  $O_i^{XY} = \cos(2\kappa_i)(S_i^x S_i^y + S_i^y S_i^x) - \sin(2\kappa_i)\{(S_i^x)^2 - (S_i^y)^2\}$ . The  $x$ ,  $y$  and  $z$  axes in the Hamiltonian (1) are along the crystallographic  $a$ -,  $b$ - and  $c$ -axes, respectively, as shown in Fig. 1(b).  $\kappa_i$  is a tilt angle of the  $\text{MnO}_4$  tetrahedron from the crystallographic  $[110]$  direction as shown in Fig. 1(a). The first and the second terms are the nearest-neighbor intra- and interplane interactions of the square lattice, respectively. The third term is a single-ion anisotropy of an easy-plane type, with  $D > 0$ , and the fourth is a Zeeman term.  $\mathcal{H}_N$  is the spin-nematic interaction, which produces the biaxial anisotropy in the  $ab$  plane [10, 11]. Note that a single-ion anisotropy with the second order of spin operators is not allowed in the  $ab$  plane due to the fourfold rotational symmetry. The lowest order in-plane single-ion anisotropy is of the fourth order and the reason it is not included is explained in the end of the supplementary sections I. Figure 2(b) shows the calculated angle dependence of  $dM/dH$  using  $J_N = 0.12$  neV and  $g\mu_B\langle S \rangle = 4.66 \mu_B$ , which reasonably reproduces the experimental data at 1.8 K in Fig. 2(a). By using  $H_{\text{SF}}$  and  $g\mu_B\langle S \rangle$  measured at each temperature we can estimate an effective  $J_N(T)$ . We find that  $J_N$  as well as  $H_{\text{SF}}$  is strongly dependent on  $T$  [Supplementary Fig. S5] and it cannot be explained solely by the change of  $g\mu_B\langle S \rangle$ . The details of the calculation are described in the supplementary sections I and II.

Based on the spin-wave calculation, the gap energies of the magnetic anisotropy at the magnetic  $\Gamma$ -point are  $\Delta_1^{\text{SWT}} \sim 16\langle S(T) \rangle^2 \sqrt{J_N(T)(2J_1 + J_2 + D/2)}$  for the  $T_1$  mode and  $\Delta_2^{\text{SWT}} = 4\langle S(T) \rangle \sqrt{D(2J_1 + J_2)}$  for the  $T_2$  mode.  $\Delta_1^{\text{SWT}}$  can be calculated by using the

values of  $J_N(T)$  from  $dM/dH$  curve and  $\langle S(T) \rangle$  from the neutron scattering experiment in the present study, and those of  $J_1$ ,  $J_2$  and  $g$  in the previous study [20]. The obtained  $T$  dependence of  $\Delta_1^{\text{SWT}}$  in Fig. 4(b), however, is not consistent with  $E_{g1}$ , particularly in the low  $T$  region. Here we note that a Mn atom has a nuclear spin  $I = 5/2$  and that the hyperfine coupling between nuclear and electron spins induces a low energy gap [24] in addition to the magnetic anisotropy gap. The energy gap induced by the hyperfine coupling has no  $\mathbf{q}$ -dependence. Then the magnon dispersion relation is modified;  $(\hbar\omega_i(\mathbf{q}))^2 = (\hbar\omega_i^{\text{SWT}}(\mathbf{q}))^2 + (\Delta^{\text{HF}})^2$  where  $\hbar\omega_i^{\text{SWT}}(\mathbf{q})$  is the pure magnon dispersion for  $T_i$  mode ( $i = 1, 2$ ) and  $\Delta^{\text{HF}}$  is the hyperfine gap [25]. The two gaps  $E_{g1}$  and  $E_{g2}$  at  $\mathbf{Q} = (1, 0, 1/2)$  are described as  $E_{g1}^2 = (\Delta_1^{\text{SWT}})^2 + (\Delta^{\text{HF}})^2$  and  $E_{g2}^2 = (\Delta_2^{\text{SWT}})^2 + (\Delta^{\text{HF}})^2$ , where  $\Delta^{\text{HF}} = \sqrt{(\chi_n(T)/\chi_c)Ag\mu_B\langle S(T) \rangle}$ . Here  $\chi_n(T)$  is the paramagnetic nuclear spin susceptibility following Curie law,  $\chi_c$  is the electron spin susceptibility along the crystallographic  $c$  direction, and  $A$  is the hyperfine coupling. In order to estimate  $\Delta^{\text{HF}}$  and  $D$ , we fit the constant- $\mathbf{q}$  cut in Fig. 3(f) to the calculated magnon cross-section. The fit to the data is good as shown by black solid curves. The  $T_1$  and  $T_2$  modes in Figs. 3(b)-3(e) are reasonably reproduced by the calculated magnon-dispersions shown by the white curves. The obtained hyperfine coupling constant is  $A = 240$  kOe as described in the supplementary section IV, and it is consistent with Ref. [25] and the value reported in  $^{55}\text{Mn}^{2+}$  ions in  $\text{ZnF}_2$  [26]. The  $T_1$  mode is, thus, hybridized with the nuclear spin. The  $T$  dependence of  $\Delta^{\text{HF}}$  is shown in Figs. 4(a) and 4(b), and that of  $\Delta_2^{\text{SWT}}$  is shown in Fig. 4(a).

$T$  dependences of  $\Delta_1^{\text{SWT}}$ , a scaled electric polarization  $P$  [9] and the second power of the scaled sublattice moment  $(g\mu_B\langle S \rangle)^2$  are shown in Fig. 4(c). We find that  $\Delta_1^{\text{SWT}}$  does not scale as  $(g\mu_B\langle S \rangle)^2$ , but is rather consistent with the temperature dependence of electric polarization,  $P$ . To discuss the behavior, we rewrite the formula of  $\mathcal{H}_N$  in equation (2) in terms of  $P$ . From the local relation between  $\mathbf{S}$  and  $\mathbf{P}$ , one has,  $P_i^Z = \Lambda_Z O_i^{XY}$  [10, 11]. This relation leads to  $\mathcal{H}_N = \sum_{i,j} J_N O_i^{XY} O_j^{XY} = \sum_{i,j} J_P P_i^Z P_j^Z$ , where  $J_P$  is an effective interaction between the electric polarizations;  $J_P = J_N/\Lambda_Z^2$ . By considering the structures of the spin and electric polarization at  $T < T_N$ , we obtain  $\Delta_1^{\text{SWT}} = 16\langle P(T) \rangle \sqrt{J_P(2J_1 + J_2 + 1/2D)}/\sin(2\kappa)$ . The fact that the magnetic anisotropy gap,  $\Delta_1^{\text{SWT}}(T)$ , is scaled by the electric polarization,  $P(T)$ , means that  $P$  induces an emergent magnetic field. In addition we notice that  $J_P$  is  $T$ -independent. Drastic  $T$  dependence of  $J_N$  thus results from the change of  $\Lambda_Z$  with  $T$ ; the modification of the hybridized orbitals of  $\text{Mn}^{2+}$  and  $\text{O}^{2-}$  ions with  $T$  leads to a small change

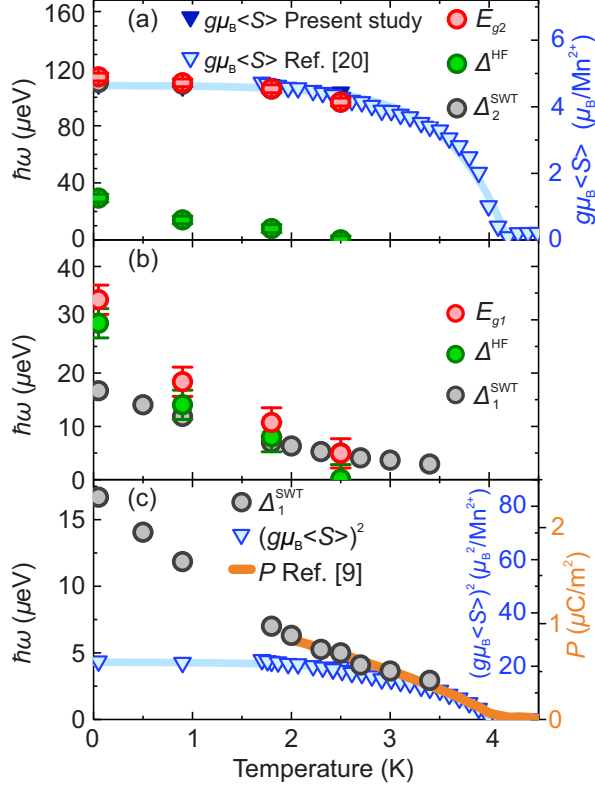


FIG. 4: The temperature dependences of gap energies observed in INS spectra, anisotropy energies, sublattice moment and electric polarization. (a)  $T$  dependences of  $E_{g2}$  (red circles),  $\Delta_2^{\text{SWT}}$  (black circles),  $\Delta^{\text{HF}}$  (green circles) and sublattice moment (blue triangles from the present study and light blue ones from the previous study [20]).  $E_{g2}$ ,  $\Delta_2^{\text{SWT}}$ , and the sublattice moment are superimposed. The light blue curve is the guide to the eyes. (b)  $T$  dependences of  $E_{g1}$  (red circles),  $\Delta_1^{\text{SWT}}$  (black circles) and  $\Delta^{\text{HF}}$  (green circles). (c)  $T$  dependences of  $\Delta_1^{\text{SWT}}$  (black circles), electric polarization  $P$  (orange curve from Ref. [9]) and the second power of the sublattice moment (light blue triangles). The sublattice moment in this panel is a combination of measurements from the present and previous [20] studies in panel (a). Vertical error bars for  $E_{g1}$ ,  $E_{g2}$  and  $\Delta^{\text{HF}}$  in panels (a) and (b) indicate the experimental resolution of the spectrometer estimated at an elastic condition.

of the energy, which is negligible in highly anisotropic system but is enhanced in the nearly isotropic system such as the symmetric half-filled shell of  $\text{Mn}^{2+}$  ion, and it is probed as the change of  $J_N$  thorough SOC. Since the change of the hybridized  $d$ - $p$  orbital with  $T$  explicitly affects the anisotropy gap of the acoustic magnon, we call it *hybridized magnon* with the  $d$ - $p$  orbital. This is a characteristic quasiparticle of the multiferroics originating from the

hybridization of spin and orbital momenta.

In contrast to  $\Delta_1^{\text{SWT}}$ , the  $T$  dependence of  $\Delta_2^{\text{SWT}}$  is almost flat at  $T \leq 2.5$  K, and the scaled  $\Delta_2^{\text{SWT}}$  is proportional to  $g\mu_B\langle S \rangle$  as shown in Fig. 4(a). The result suggests that  $D$  is essentially temperature independent. This is consistent with the dependence  $\Delta_2^{\text{SWT}} = 4\langle S(T) \rangle \sqrt{D(2J_1 + J_2)}$  describing conventional antiferromagnets in which a single-ion anisotropy is represented by the quadratic form of the spin operator [18, 19].

Now we compare the electric dipole energy of  $\text{Ba}_2\text{MnGe}_2\text{O}_7$  as a dielectric with that as a multiferroic. The former energy is estimated by the formula of the classical electromagnetism,  $U_{(1,2)} = 1/(4\pi\epsilon_0\epsilon r^3)(\mathbf{P}_1 \cdot \mathbf{P}_2 - 3(\mathbf{P}_1 \cdot \hat{\mathbf{r}})(\mathbf{P}_2 \cdot \hat{\mathbf{r}}))$ . The reported electric polarization is  $(0, 0, p_c)$  with  $p_c \sim 0.8 \mu\text{C}/\text{m}^2$  at 2.0 K in the magnetic field of 1 T applied along the [110] direction [9]. The dielectric permittivity is  $\epsilon \sim 14$  [23]. We assume that the polarization is localized at each  $\text{Mn}^{2+}$  ion. By summing up the pairs of the nearest-neighbor  $\text{Mn}^{2+}$  ions in the  $ab$  plane and those along the  $c$  axis,  $U_{(1,2)}$  per  $\text{Mn}^{2+}$  ion is estimated to be  $-0.54$  peV. Next we estimate the electric dipole energy as a multiferroic system, where both dielectric and magnetic energies are renormalized. In  $\text{Ba}_2\text{MnGe}_2\text{O}_7$  the spin-nematic operator is equivalent to the electric polarization, and only the component  $P_i^Z = \Lambda_Z O_i^{XY}$  is active in the ordered state. Then the renormalized dipole energy is  $E_{(1,2)} = J_P P_1^Z P_2^Z = J_N O_1^{XY} O_2^{XY}$  at 1.8 K by using  $J_N$  and  $g\mu_B\langle S \rangle$  obtained in the present study. Note that the spin moment points along the  $a$  or  $b$  direction in the ordered state,  $E_{(1,2)}$  per  $\text{Mn}^{2+}$  ion is estimated to be  $-7.95$  neV. The renormalized dipole energy in  $\text{Ba}_2\text{MnGe}_2\text{O}_7$  is gigantic compared with the classical dipole energy. For the control of the electric polarization, the required electric field is much stronger than that estimated from the classical electromagnetism. The electric polarization in spin-driven multiferroics is, thus, robust to the external electric field.

In conclusion, we found that the temperature dependence of the magnetic anisotropy energy in the multiferroic  $\text{Ba}_2\text{MnGe}_2\text{O}_7$  is scaled by the electric polarization. The change of the hybridized orbitals of the metal and the ligands with the temperature determines the spin-nematic interaction, leading to nontrivial temperature dependence of the anisotropy energy in the neutron spectrum as well as that of the spin-flop field. The effect of hyperfine coupling between nuclear and electron spins is also observed in the low temperature region. Thorough account for this effect is important for accurate understanding of the temperature

evolution of the electronic spin gap.

---

- [1] Y. Tokura, S. Seki, and N. Nagaosa, *Rep. Prog. Phys.* **77**, 076501 (2014).
- [2] S. Dong, J.-M. Liu, S.-W. Cheong, and Z. Ren, *Adv. Phys.* **64**, 519 (2015).
- [3] M. Fiebig, T. Lottermoser, D. Meier, and M. Trassin, *Nat. Rev. Mater.* **1**, 16046 (2016).
- [4] T. Kimura, T. N. Goto, H. Shintani, K. Ishizaka, T. Hisa Arima, and Y. Tokura, *Nature* **426**, 55 (2003).
- [5] H. Katsura, N. Nagaosa, and A. V. Balatsky, *Phys. Rev. Lett.* **95**, 057205 (2005).
- [6] S.-W. Cheong and M. Mostovoy, *Nat. Mater.* **6**, 13 (2007).
- [7] T.-h. Arima, *Journal of the Physical Society of Japan* **76**, 073702 (2007).
- [8] C. Jia, S. Onoda, N. Nagaosa, and J. H. Han, *Phys. Rev. B* **74**, 224444 (2006).
- [9] H. Murakawa, Y. Onose, S. Miyahara, N. Furukawa, and Y. Tokura, *Phys. Rev. B* **85**, 174106 (2012).
- [10] J. Romhányi, M. Lajkó, and K. Penc, *Phys. Rev. B* **84**, 224419 (2011).
- [11] M. Soda, M. Matsumoto, M. Månsson, S. Ohira-Kawamura, K. Nakajima, R. Shiina, and T. Masuda, *Phys. Rev. Lett.* **112**, 127205 (2014).
- [12] S. Seki, X. Z. Yu, S. Ishiwata, and Y. Tokura, *Science* **336**, 198 (2012).
- [13] J. S. White, K. Prša, P. Huang, A. A. Omrani, I. Živković, M. Bartkowiak, H. Berger, A. Magrez, J. L. Gavilano, G. Nagy, J. Zang, and H. M. Rønnow, *Phys. Rev. Lett.* **113**, 107203 (2014).
- [14] A. I. Popov, D. I. Plokhov, and A. K. Zvezdin, *Phys. Rev. B* **87**, 024413 (2013).
- [15] T. Kurumaji, K. Ohgushi, and Y. Tokura, *Phys. Rev. B* **89**, 195126 (2014).
- [16] S. Hayashida, M. Soda, S. Itoh, T. Yokoo, K. Ohgushi, D. Kawana, H. M. Rønnow, and T. Masuda, *Phys. Rev. B* **92**, 054402 (2015).
- [17] M. Soda, S. Hayashida, B. Roessli, M. Månsson, J. S. White, M. Matsumoto, R. Shiina, and T. Masuda, *Phys. Rev. B* **94**, 094418 (2016).
- [18] F. M. Johnson and A. H. Nethercot, *Phys. Rev.* **114**, 705 (1959).
- [19] R. J. Birgeneau, J. Skalyo, and G. Shirane, *Phys. Rev. B* **3**, 1736 (1971).
- [20] T. Masuda, S. Kitaoka, S. Takamizawa, N. Metoki, K. Kaneko, K. C. Rule, K. Kiefer, H. Manaka, and H. Nojiri, *Phys. Rev. B* **81**, 100402(R) (2010).

- [21] A. Sazonov, V. Hutanu, M. Meven, G. Roth, R. Georgii, T. Masuda, and B. Náfrádi, *Inorganic Chemistry* **57**, 5089 (2018).
- [22] K. Shibata, N. Takahashi, Y. Kawakita, M. Matsuura, T. Yamada, T. Tominaga, W. Kambara, M. Kobayashi, Y. Inamura, T. Nakatani, K. Nakajima, and M. Arai, *JPS Conference Proceedings* **8**, 036022 (2015).
- [23] Y. Iguchi, Y. Nii, M. Kawano, H. Murakawa, N. Hanasaki, and Y. Onose, *Phys. Rev. B* **98**, 064416 (2018).
- [24] A. S. Borovik-Romanov and V. Tulin, *Journal of Experimental and Theoretical Physics Lett.* **1**, 134 (1965).
- [25] I. A. Zaliznyak, N. N. Zolin, and S. V. Petrov, *Journal of Experimental and Theoretical Physics Lett.* **64**, 473 (1996).
- [26] A. M. Clogston, J. P. Gordon, V. Jaccarino, M. Peter, and L. R. Walker, *Phys. Rev.* **117**, 1222 (1960).

## **Acknowledgements**

We are grateful to Mr. T. Asami for supporting us in the neutron scattering experiment. The neutron experiment at the Materials and Life Science Experimental Facility of the J-PARC was performed under a user program (Proposal No. 2016B0140). S. Hasegawa and S. Hayashida were supported by the Japan Society for the Promotion of Science through the Leading Graduate Schools (MERIT). This project is supported by JSPS KAKENHI Grant Numbers 19KK0069 and 20K20896, and by US-Japan collaboration program.